This is a preprint, the final version is subject to change, of the American Mineralogist (MSA)
Cite as Authors (Year) Title. American Mineralogist, in press.
(DOI will not work until issue is live.) DOI: http://dx.doi.org/10.2138/am-2017-5837

Revision 3 of manuscript #5837

Compressibility and high-pressure structural behavior of $Mg_2Fe_2O_5$

Nicki C. Siersch[1], Tiziana Boffa Ballaran[1], Laura Uenver-Thiele[2], Alan B. Woodland[2]

[1]Bayerisches Geoinstitut, Universität Bayreuth, D-95440 Bayreuth, Germany

[2]Institut für Geowissenschaften, Goethe-Universität Frankfurt, Altenhöferallee 1, D-60438 Frankfurt am Main, Germany

Abstract

The compressibility and structural behavior of the novel $Mg_2Fe_2O_5$ oxide has been investigated by in-situ single-crystal X-ray diffraction in a diamond anvil cell up to a pressure of 17 GPa. The bulk compressibility of $Mg_2Fe_2O_5$ can be described using a second-order Birch-Murnaghan equation of state (BM2 EoS) with V_0 = 352.4(2) Å^3 and K_0 = 171(4) GPa. Three linear BM2 EoS were used to describe the axial compressibility of $Mg_2Fe_2O_5$, which was found to be highly anisotropic. The *a* and *b* lattice parameters have very similar compressibilies, with a_0 = 2.8917(11) Å and linear modulus M_a = 572(16) GPa and b_0 = 9.736(3) Å and linear modulus M_b = 583(15) GPa, respectively. The *c*-axis is the most compressible direction as indicated by the smaller linear modulus (c_0 = 12.520(15) Å and M_c = 404(28) GPa). The $Mg_2Fe_2O_5$ structure consists of edge-sharing octahedra alternating with layers of trigonal prisms. The compression behavior of the M-O bonds of the M1 and M2 octahedra and of the M3 prisms depend on their location in either an edge-sharing environment, which makes them stiffer, or a corner-sharing environment where they have more freedom to distort and compress. The main compression mechanism consists of a

polyhedral tilting around the M2-O1-M2 angle, which decreases with increasing pressure. $Mg_2Fe_2O_5$ has recently been added to the list of stable endmembers of phases with M_4O_5 stoichiometry, making it a potentially relevant phase in the Earth's upper mantle and transition zone. In order to develop thermodynamic activity-composition models for high-pressure phases, it is crucial to know the accurate elastic parameters of each individual endmember. Currently these have only been measured for $Mg_2Fe_2O_5$ (this study) and Fe_4O_5.

Keywords: $Mg_2Fe_2O_5$, Fe_4O_5, transition zone, high-pressure, compressibility, crystal structure

INTRODUCTION

A novel oxide phase, Fe_4O_5, was recently discovered to be stable at upper mantle and transition zone conditions through the oxidation of siderite (Lavina et al. 2011) or the breakdown of magnetite (Woodland et al. 2012). More recently, Myhill et al. (2016) combined experimental observations with thermodynamic models and confirmed the stability of Fe_4O_5 between 8 and 22 GPa. Also, other spinel-structured phases such as chromite ($FeCr_2O_4$), Mg-chromite ($MgCr_2O_4$) and magnesioferrite ($MgFe_2O_4$) have been found to break down to $Fe_2Cr_2O_5$ + Cr_2O_3 (Ishii et al. 2014), $Mg_2Cr_2O_5$ + Cr_2O_3 (Ishii et al. 2015) and $Mg_2Fe_2O_5$ + Fe_2O_3 (Uenver-Thiele et al. 2014), respectively, at conditions similar to those reported for magnetite. Among these four endmembers the $Fe^{3+}/\sum Fe$ varies between 0 and 1.0 making these phases stable over a large range of oxygen fugacities, fO_2. Moreover, solid solutions between Fe_4O_5 and $Fe_2Cr_2O_5$ or $Mg_2Fe_2O_5$ have also been reported (Woodland et al. 2013), suggesting that these novel oxides with M_4O_5 stoichiometry may be relevant for the mineralogy of parts of the Earth's upper mantle and transition zone. Knowledge of the elastic parameters of these phases is thus crucial for constraining their properties and predicting their stability. So far, elastic parameters have only been obtained for Fe_4O_5 (Lavina et al. 2011) and

these were used in the recent thermodynamic activity-composition model for Fe_4O_5–$Mg_2Fe_2O_5$ binary solid solutions (Myhill et al. 2016) with the assumption that the elastic behavior of the two end-members was identical. However, it is very likely that the elastic properties for $Mg_2Fe_2O_5$ differ significantly from those of the Fe-endmember in a fashion similar to that observed for the analog spinel-structured phases. For example, magnetite has a larger bulk modulus (198 GPa, Haavik et al. 2000) than that reported for magnesioferrite (177.7 GPa, Levy et al. 2004).

At ambient conditions $Mg_2Fe_2O_5$ is isostructural with Fe_4O_5 (orthorhombic with space group *Cmcm*), but it has smaller lattice parameters: a = 2.8889(4), b = 9.7282(4) and c = 12.5523(7) Å (Boffa Ballaran et al. 2015). Its structure consists of layers of edge-sharing octahedra (M1 and M2) alternating with layers of trigonal prisms M3 (Fig. 1). Mg and Fe can occupy all three crystallographic sites M1, M2 and M3, although Mg prefers the M3 site (Boffa Ballaran et al. 2015). The cation that occupies the M3 site is responsible for the height of the trigonal prism expressed as the O3-O3 (O1-O1) interatomic distances, and consequently, the corresponding a-parameter. Given that Mg is smaller than Fe^{2+}, the shorter a-axis is in agreement with the preference of this cation for the M3 site (Boffa Ballaran et al. 2015). It has also been found that the substitution of Mg at the M1 and M2 sites reduces the octahedral distortion (Boffa Ballaran et al. 2015) observed in the pure Fe_4O_5 endmember (Lavina et al. 2011). The structural differences between the two end-members can be expected to influence their compression behavior. Therefore, the aim of this study is to determine the equation of state parameters of $Mg_2Fe_2O_5$ and to characterize its structural changes as a function of pressure by means of high-pressure single-crystal X-ray diffraction.

METHODS

Sample characterization

$Mg_2Fe_2O_5$ was synthesized in a multi-anvil apparatus using a stoichiometric mixture of MgO and $MgFe_2O_4$ along with some PtO_2 to keep the oxygen fugacity high. The experimental setup is described in detail by Boffa Ballaran et al. (2015). Microprobe analysis confirmed a complete substitution of Mg^{2+} for Fe^{2+}, suggesting that all Fe is trivalent (Boffa Ballaran et al. 2015). A crystal with dimensions 100 x 70 x 90 μm^3 and relatively sharp ω diffraction profiles with full width at half maximum of 0.12 - 0.15° was chosen to be double-sided polished to a thickness of 17 μm. After polishing, the diffraction profiles were measured again to ensure that the quality of the crystal was maintained.

High-pressure experiments

The thin crystal of $Mg_2Fe_2O_5$ was loaded into a piston-cylinder diamond anvil cell (DAC) (Kantor et al. 2012) equipped with Boehler-Almax diamonds (culet size of 400 μm) glued onto tungsten carbide seats. A rhenium (Re) gasket with an original thickness of 200 μm was pre-indented to a thickness of 76 μm and a hole with a diameter of 250 μm was drilled. The sample was placed at the center of the hole, right next to a 10 μm diameter ruby sphere, which was used to monitor the pressure. The cell was loaded with neon (Ne) gas as pressure-transmitting medium using the gas-loading system installed at BGI (Kurnosov et al. 2008). After each pressure increase, the pressure inside the cell was left to stabilize for at least one day to avoid changes in pressure during the measurements. A Raman micro-spectrometer equipped with a He-Ne-laser (λ = 632.8 nm) with 20 mW laser power was used to measure the fluorescence bands of the ruby sphere inside the DAC before and after the X-ray diffraction measurements. A ruby chip also was measured each time at ambient conditions as a reference. Pressures were calculated using the ruby fluorescence calibrations of Mao et al. (1986) and Dewaele et al. (2004) (Tab. 1). The two sets of values are identical within the

uncertainties. Data analysis was carried out using the pressures obtained from the calibration of Dewaele et al. (2004).

Single-crystal X-ray diffraction

High-pressure X-ray diffraction experiments were performed using an Oxford Xcalibur diffractometer using MoKα radiation (λ = 0.70937 Å) operated at 50 kV and 40 mA and equipped with a graphite monochromator and a Sapphire 2 CCD area detector. The single-crystal data were collected at each pressure using ω scans with a step size of 0.25° and a default time of 60 s in a 2θ range between 2 and 70° by measuring several redundant reflections. The intensity data were integrated using the Crysalis Pro 171.37.35 software in which Lorentz and polarization factor corrections are included. The unit-cell lattice parameters were obtained up to 17.06(5) GPa from the intensity data using an average number of 250 reflections at each pressure (Tab. 1). An analytical absorption correction was performed for each set of data in order to take into account not only the absorption of the sample (8.8 cm^{-1}), but also that of the diamond anvils having an absorption coefficient of 2.03 cm^{-1} (Creagh and Hubbell 1992), as well as that of the Re gasket, which can absorb up to 90% of the MoKα radiation (Angel 2004). To this end, the Absorb6.0 package (Angel 2004) integrated into the Crysalis absorption correction software was used in order to calculate the difference between the path of the incident and the diffracted beam on the basis of the shape of the sample and its position in the gasket hole.

The corrected intensity data were then used for structural refinements performed with the ShelX sofware (Sheldrick 2008) integrated in the WinGX program system (Farrugia 1999) with neutral scattering factors for Mg, Fe and O. Isotropic displacement parameters were used in order to reduce the number of variables due to the limited coverage of the reciprocal space resulting from the geometry of the DAC setup. The occupancies of Mg/Fe at the M1, M2 and

M3 sites were fixed to the values reported by Boffa Ballaran et al. (2015), namely 53%, 30% and 86% of Mg, respectively, because it was assumed that the occupancies of the three different sites do not change with increasing pressure at room temperature. Between 90 and 112 unique reflections were available at each pressure for the refinement of 15 parameters. Details of the structural refinements are reported in the CIF-file. Atomic coordinates and isotropic displacement parameters are given in Table 2.

RESULTS AND DISCUSSION

Compressibility of $Mg_2Fe_2O_5$

The variations with pressure of the unit-cell volume and unit-cell axes of $Mg_2Fe_2O_5$ are shown in Figure 2a and 2b, respectively. These decrease continuously as a function of pressure and no evidence of a phase transition was found up to 17 GPa (i.e. the maximum pressure reached in this study). The uncertainties associated with the *c*–axis parameter are larger than those obtained for the *a* and *b*–axes due to the orientation of the crystal in the DAC. The normalized pressure F_E versus the Eulerian strain f_E plot was calculated for the Birch-Murnaghan equation of state (Angel 2000) in order to obtain a visual assessment of the significance of higher-order terms in the Helmholtz energy used to derive the BM parameters. The data points of the *F-f* plot obtained for $Mg_2Fe_2O_5$ (Fig. 3) can be fitted taking into account their uncertainties by the equation $F_E = 168(14) + 118(590)\, f_E$. The large uncertainty of the slope, much larger than its value clearly indicates that the data can be fitted equally well with a horizontal line, and thus a second-order truncation of the strain energy is sufficient for describing the *P-V* data. Consequently, a second-order Birch-Murnagham equation of state (BM2 EoS) was used to fit the *P-V* data of $Mg_2Fe_2O_5$ (Fig. 2a) with the program EoSfitGUI (Angel et al. 2014). The room-pressure volume, V_0, and the room-pressure isothermal bulk

147 modulus, K_{T0}, were refined simultaneously resulting in the following values (Tab. 3): V_0 =
148 352.4(2) Å^3 and K_0 = 171(4) GPa. Also the three unit-cell axes were fit using linearized BM2
149 EoS according to the procedure described by Angel et al. (2014). The room pressure values of
150 the *a*-, *b*- and *c*-axes and their respective linear moduli, M_0, obtained using the program
151 EoSfitGUI (Angel et al. 2014) also are reported in Table 3. The *a* and *b*-axes have similar
152 compressibilies with a_0 = 2.8917(11) Å and a linear modulus M_a = 572(16) GPa and b_0 =
153 9.736(3) Å and a linear modulus M_b = 583(15) GPa, respectively. The *c*-axis is the most
154 compressible direction (Fig. 2b) with c_0 = 12.520(15) Å and a linear modulus M_0 = 404(28)
155 GPa.

156

157 **Structural behavior of $Mg_2Fe_2O_5$ with pressure**

158 The dense $Mg_2Fe_2O_5$ structure, which is made of edge-sharing octahedra, has one degree of
159 freedom that is represented by the M2-O1-M2 angle formed by corner-sharing M2 octahedra
160 through the O1 atoms (Fig. 1). This angle decreases with pressure (Fig. 4a and Tab. 4) and, as
161 a consequence, the interatomic distance of the O3 atoms of two adjacent M2 octahedra also
162 decreases with increasing pressure at a much faster rate than the distances between adjacent
163 oxygens belonging to the same M2 octahedral site. These distances are plotted for comparison
164 in Figure 4b. This is quite remarkable, considering the short O3-O3 interatomic distance even
165 at ambient conditions (2.662(10) Å) (Fig. 4b). The variation of the M2-O1-M2 angle may be
166 responsible, at least in part, for the larger compression of the *c*-axis, since it lies along this
167 direction.

168 The elastic parameters of the individual bond distances of the M1, M2 and M3 polyhedra
169 have been determined by fitting their variation as a function of pressure with a linearized
170 BM2 EoS using the program EoSfitGUI (Angel et al. 2014) and are reported in Table 5. The
171 M1 octahedron consists of two shorter bond distances M1-O3 that lie slightly inclined with

respect to the *c*-axis, and four longer distances M1-O2, which are almost perpendicular to the *c*-axis (Fig. 1). The two sets of distances have a similar compressibility within their uncertainties (Fig. 5a), having linear moduli of 447(63) GPa and 517(33) GPa, respectively. The M1 octahedral distortion remains the same at all pressures, as indicated by only minor variations in the octahedral quadratic elongation (OQE) and octahedral angle variance (OAV) (Robinson et al. 1971) (Tab. 4).

The M2 site has a much larger distortion than the M1 site (Tab. 4), since one of the bond lengths (M2-O2b) of the octahedral coordination is much longer than the other five (Evrard et al., 1980; Boffa Ballaran et al. 2015). Such distortion is retained with increasing pressure due to a very anisotropic compression of the M2-O bonds. Here, the longest M2-O2b bond distance (M_0 = 363(58) GPa) and the shortest M2-O1 bond distance (M_0 = 484(43) GPa) are much more compressible than the M2-O2 and M2-O3 bond distances (M_0 = 753(77) GPa and M_0 = 782(60) GPa, respectively) (Fig. 5b). The large compressibility of the M2-O1 bond distance in spite of its quite short room-pressure value is likely due to the fact that the O1 oxygen is under-bonded, being the only corner-sharing oxygen. Note also that the M2-O1 and M2-O2b bonds lie only slightly inclined with respect to the *c*-axis and, therefore, may play a role in its larger compressibility. The M2-O2 and M2-O3 bond distances (Fig. 5b) are the least compressible bonds in the $Mg_2Fe_2O_5$ structure.

The M3 prism has two non-equivalent bond distances (Fig. 5c). The M3-O3 bond distance exhibits the largest compressibility of the $Mg_2Fe_2O_5$ structure, with a linear modulus of 323(22) GPa, whereas the shorter M3-O1 is less compressible (M_0 = 587(40) GPa).

IMPLICATIONS

$Mg_2Fe_2O_5$ has recently been added to the list of stable endmembers of post-spinel-structured phases with M_4O_5 stoichiometry (Woodland et al. 2013, Uenver-Thiele et al. 2014). To be able to develop thermodynamic activity-composition models it is crucial to know the exact elastic parameters of each individual endmember, and up to now only data for Fe_4O_5 has been reported (Lavina et al. 2011 and see Tab. 3). Studies of spinel-structured phases already indicated that there are significant differences in the bulk moduli of Fe^{2+}-bearing phases compared to their Mg-bearing counterparts (Haavik et al. 2000, Levy et al. 2004). This can now be extended to post-spinel-structured phases. In this study, the elastic parameters for $Mg_2Fe_2O_5$ were obtained up to 17.06(5) GPa (Tab. 3). Figure 6 shows a direct comparison between the BM2 EoS of Fe_4O_5 (Lavina et al. 2011) and $Mg_2Fe_2O_5$. $Mg_2Fe_2O_5$ is clearly more compressible than Fe_4O_5, as it has a lower bulk modulus (171(4) GPa compared to 185.7 GPa) (note that in the original paper, Lavina et al. (2011) do not report the uncertainties associated with the calculated bulk modulus). This trend is consistent with that observed for the analog spinel-structured phases (Haavik et al. 2000, Levy et al. 2004). The difference between the two bulk moduli of 14.7 GPa is larger than the uncertainty reported for $Mg_2Fe_2O_5$ and therefore needs to be taken into account when modelling the thermodynamic properties of oxide solid solutions under mantle conditions since it may influence their stability and properties (eg. Myhill et al. 2016). Fe-bearing phases with M_4O_5 stoichiometry are relevant phases of the Earth's upper mantle and transition zone due to formation of solid solutions with Mg and Cr substituting for Fe^{2+} and Fe^{3+}, respectively (Woodland et al. 2013, Ishii et al. 2014, 2015), making them stable over a large range of oxygen fugacities. Recently, Wirth et al. (2014) reported a Fe^{3+}-rich magnesioferrite $(Mg_{0.42}Fe_{0.58})Fe_2O_4$ coexisting with ferropericlase (Mg,Fe)O and blebs of Fe-Ni alloy in a diamond host possibly from the lower mantle. The magnesioferrite was suggested to be exsolved from the original pure (Mg,Fe)O inclusion during upwelling in a plume (Wirth et al. 2014). At pressures and temperatures of the transition zone, this Fe^{3+}-rich magnesioferrite most likely was stable as $Mg_2Fe_2O_5$ + Fe_2O_3,

making the Mg-endmember $Mg_2Fe_2O_5$ a relevant phase of the transition zone and the lower upper mantle.

Acknowledgements

This study was supported by grants from the Deutsche Forschungsgemeinschaft (DFG) to T.B.B. (BO-2550/7-1) and A.B.W. (WO652/20-1). The authors would like to thank Hubert Schulze and Raphael Njul for the preparation of the sample. We thank Steve Jacobsen and an anonymous reviewer for their comments which helped us to improve the manuscript.

References

Angel, R. (2000) Equations of State. Reviews in Mineralogy and Geochemistry, 41, 35-59.

Angel, R. (2004) Absorption corrections for diamond-anvil pressure cells implemented in the software package Absorb6.0. Journal of Applied Crystallography, 37, 486-492.

Angel, R., Gonzalez-Platas, J., and Alvaro, M. (2014). EosFit7c and a Fortran module (library) for equation of state calculations. Zeitung für Kristallographie, 229(5), 405-419.

Boffa Ballaran, T., Uenver-Thiele, L., and Woodland, A. (2015) Complete substitution of Fe^{2+} by Mg in Fe_4O_5: The crystal structure of the $Mg_2Fe_2O_5$ end-member. American Mineralogist, 100, 628-632.

Creagh, D., and Hubbell, J. (1992) X-ray absorption (or attenuation) coefficients. In E. Prince, Ed., International Tables of Crystallography, Vol. C, p. 220-230. Kluwer Academic Publishers, Dordrecht.

Dewaele, A., Loubeyre, P., and Mezouar, M. (2004) Equations of state of six metals above 94 GPa. Physical Review, B 70, 094112-1-094112-8.

Evrard, O., Malaman, B., Jeannot, F., Courtois, A., Alebouyeh, H., and Geradin, R. (1980) Mise en évidence de $CaFe_4O_6$ et détermination des structures cristallines des derrites de calcium $CaFe_{2+n}O_{4+n}$ (n=1, 2, 3): nouvel exemple d'intercroissance. Journal of Solid State Chemistry, 35, 112-119.

Farrugia, L. (1999) *WinGX* suite for small-molecule single-crystal crystallography. Journal of Applied Crystallography, 32, 837-838.

Haavik, C., Stolen, S., Fjellvag, H., Hanfland, M., and Häusermann, D. (2000) Equation of state of magnetite and its high-pressure modifications. American Mineralogist, 85, 514-523.

Ishii, T., Kojitani, H., Tsukamoto, S., Fujino, K., Mori, D., Inaguma, Y., Tsuino, N., Yoshino, T., Yamazaki, D., Higo, Y., Funakoshi, K., and Akaogi, M. (2014) High-pressure phase transition in $FeCr_2O_4$ and structure analysis of new post-spinel $FeCr_2O_4$ and $Fe_2Cr_2O_5$ phases with meteoritical and petrological implications. American Mineralogist, 99, 1788-1797.

Ishii, T., Kojitani, H., Fujino, K., Yusa, H., Mori, D., Inaguma, Y., Matsushita, Y., Yamaura, K., and Akaogi, M. (2015) High-pressure high-temperature transitions in $MgCr_2O_4$ and crystal structures of new $Mg_2Cr_2O_5$ and post-spinel $MgCr_2O_4$ phases with implications for ultrahigh-pressure chromitites in ophiolites. American Mineralogist, 100, 59-65.

Kantor, I., Prakapenka, V., Kantor, A., Dera, P., Kurnosov, A., Sinogeikin, S., Dubrovinskaia, N., and Dubrovinsky, L. (2012) BX90: A new diamond anvil cell design for X-ray diffraction and optical measurements. Review of Scientific Instruments, 83, 125102.

Kurnosov, A., Kantor, I., Boffa-Ballaran, T., Lindhardt, S., Dubrovinsky, L., Kuznetsov, A., and Zehnder, B. (2008) A novel gas-loading system for mechanically closing of various types of diamond anvil cells. Review of Scientific Instruments, 79, DOI:10.1063/1.2902506.

Lavina, B., Dera, P., Kim, E., Meng, Y., Downs, R., Weck, P., Sutton, S., and Zhao, Y. (2011) Discovery of the recoverable high-pressure iron oxide Fe_4O_5. Proceedings of the National Academy of Sciences, 108, 17281-17285.

Levy, D., Diella, V., Dapiaggi, M., Sani, A., Gemmi, M., and Pavese, A. (2004) Equation of state, structural behaviour and phase diagram of synthetic $MgFe_2O_4$, as a function of pressure and temperature. Physics and Chemistry of Minerals, 31, 122-129.

Mao, H., Xu, J., and Bell, P. (1986) Calibration of the Ruby Pressure Gauge to 800 kbar under Quasi-Hydrostatic Conditions. Journal of Geophysical Research, 91, 4673-4676.

Myhill, R., Ojwang, D., Ziberna, L., Frost, D., Boffa Ballaran, T., and Miyajima, N. (2016) On the P-T-fO_2 stability of Fe_4O_5, Fe_5O_6 and Fe_4O_5-rich phases: a thermodynamic and experimental study. Contributions to Mineralogy and Petrology, 171:51, DOI: 10.1007/s00410-016-1258-4.

Robinson, K., Gibbs, G.V., and Ribbe, P.H. (1971) Quadratic elongation: a quantitative measure of distortion in coordination polyhedra. Science, 172, 567-570.

Sheldrick, G. (2008) A short history of SHELX. Acta Crystallographica, A64, 112-122.

Uenver-Thiele, L., Woodland, A., Boffa Ballaran, T., and Frost, D. (2014) Stability and structure of $Mg_2Fe_2O_5$ at high P-T conditions. Deutsche Mineralogische Gesellschaft Annual Meeting, Jena (abs: PHY-PO3).

Wirth, R., Dobrzhinetskaya, L., Harte, B., Schreiber, A., and Green, H.W. (2014) High-Fe (Mg,Fe)O inclusion in diamond apparently from the lowermost mantle. Earth and Planetary Science Letters, 404, 365-375.

287 Woodland, A., Frost, D., Trots, D., Klimm, K., and Mezouar, M. (2012) In situ observation of
288 the breakdown of magnetite (Fe_3O_4) to Fe_4O_5 and hematite at high pressures and
289 temperatures. American Mineralogist, 97, 1808-1811.

290 Woodland, A., Schollenbruch, K., Koch, M., Boffa Ballaran, T., Angel, R., and Frost, D.
291 (2013) Fe_4O_5 and its solid solutions in several simple systems. Contributions to Mineralogy
292 and Petrology, 166, 1677-1686.

Figure captions

Figure 1. Crystal structure of $Mg_2Fe_2O_5$ at ambient conditions. $Mg_2Fe_2O_5$ crystallizes in the *Cmcm* space group and consists of layers of edge-sharing octahedra alternating with trigonal prisms.

Figure 2. (**a**) Bulk and (**b**) axial compressibility of $Mg_2Fe_2O_5$. The bulk compressibility is highly anisotropic with the *c*-axis being the most compressible direction. The *a* and *b*-axes exhibit similar compression behavior. The solid lines represent 2nd order Birch-Murnaghan EoS fits to the data.

Figure 3. Normalized pressure F_E versus the Eulerian strain f_E calculated for the *P-V* data collected in this study. The dashed line is a weighted fit through the data points described by the equation $F_E = 168(14) + 118(590)\ f_E$. The following calculation of K' and error propagation leads to a value of $K' = 4.5(2.5)$. The large uncertainty of the slope of the linear fit indicates that the resolution of the data is not sufficient for accurately constraining the small deviation from the value of 4 of the first pressure derivative and therefore a second-order truncation of the BM EoS has been used for describing the *P-V* data.

Figure 4. (**a**) Variation of the M2-O1-M2 angle with pressure. (**b**) Compression behavior of the O3-O3, O2-O2, O1-O2 and O1-O3 interatomic distances. The distance between the O3-O3 atoms decreases rapidly in comparison to the edge-sharing O2-O2 bond and the corner-sharing O1-O2 and O1-O3 bond distances likely due to a M2-O1-M2 tilting mechanism.

Figure 5. Compression behavior of the individual bond distances of M1 (**a**), M2 (**b**) and M3 (**c**), respectively. Solid curves represent BM2 EoS fits.

Figure 6. Comparison of the BM2 EoS fits for Fe_4O_5 and $Mg_2Fe_2O_5$. The Mg-endmember is more compressible than the Fe^{2+}-end member. The solid curve represents the BM2 EoS fit to

316 $Mg_2Fe_2O_5$. The dashed curve is the BM2 EoS fit for Fe_4O_5 calculated using the parameters
317 described by Lavina et al. (2011).

318 **Table 1.** Unit-cell lattice parameters of $Mg_2Fe_2O_5$ determined by high-pressure single-crystal

319 X-ray diffraction.

pressure (GPa) Dewaele et al. 2004	pressure (GPa) Mao et al. 1986	*a* (Å)	*b* (Å)	*c* (Å)	*V* (Å^3)
0.0001(1)	0.0001(1)	2.8923(6)	9.7361(9)	12.52(3)	352.6(8)
0.70(7)	0.69(6)	2.8880(3)	9.7300(9)	12.48(3)	350.7(8)
2.15(8)	2.15(8)	2.8808(3)	9.6956(7)	12.46(2)	348.0(6)
3.82(5)	3.81(5)	2.8746(5)	9.6855(11)	12.38(4)	344.7(11)
6.36(5)	6.34(5)	2.8576(4)	9.6266(9)	12.38(3)	340.6(8)
7.27(9)	7.31(5)	2.8613(4)	9.6314(9)	12.28(3)	338.4(8)
8.48(5)	8.45(5)	2.8525(4)	9.6057(9)	12.29(3)	336.7(8)
9.97(19)	9.92(18)	2.8445(5)	9.5808(10)	12.28(4)	334.7(11)
11.63(7)	11.57(7)	2.8421(5)	9.5712(10)	12.20 (3)	331.9(8)
12.62(5)	12.54(5)	2.8348(4)	9.5507 (9)	12.18(3)	329.8(8)
13.98(10)	13.89(10)	2.8284(4)	9.5213(8)	12.20(3)	328.5(8)
16.09(7)	15.97(7)	2.8239(4)	9.5094(8)	12.11(3)	325.2(8)
17.06(5)	16.92(5)	2.8191(4)	9.4960(8)	12.10(3)	323.9(8)

320

321 **Table 2.** Atomic coordinates and displacement parameters of $Mg_2Fe_2O_5$ at each measured
322 pressure points between room pressure and 17.06(5) GPa.

	M1	M2	M3	O1	O2	O3
			0.0001(1) GPa			
x	0.0000(0)	0.0000(0)	0.0000(0)	0.0000(0)	0.0000(0)	0.0000(0)
y	0.0000(0)	0.26244(8)	0.51249(19)	0.16309(48)	0.36042(32)	0.09647(31)
z	0.0000(0)	0.11423(29)	0.2500(0)	0.2500(0)	0.54661(110)	0.64538(93)
Uiso	0.00616(28)	0.00689(58)	0.00938(27)	0.01040(130)	0.00923(108)	0.00991(89)
			0.70(7) GPa			
x	0.0000(0)	0.0000(0)	0.0000(0)	0.0000(0)	0.0000(0)	0.0000(0)
y	0.0000(0)	0.26248(7)	0.51263(16)	0.16312(27)	0.35975(27)	0.09561(27)
z	0.0000(0)	0.11505(21)	0.2500(0)	0.2500(0)	0.54573(72)	0.64596(58)
Uiso	0.00584(33)	0.00656(22)	0.00978(44)	0.01166(102)	0.00861(72)	0.051091(78)
			2.15(8) GPa			
x	0.0000(0)	0.0000(0)	0.0000(0)	0.0000(0)	0.0000(0)	0.0000(0)
y	0.0000(0)	0.26267(7)	0.51252(17)	0.16305(44)	0.35999(29)	0.09573(32)
z	0.0000(0)	0.11506(23)	0.2500(0)	0.2500(0)	0.54682(88)	0.64630(68)
Uiso	0.00594(36)	0.00616(27)	0.00798(45)	0.01061(108)	0.00854(70)	0.01105(82)
			3.82(5) GPa			
x	0.0000(0)	0.0000(0)	0.0000(0)	0.0000(0)	0.0000(0)	0.0000(0)
y	0.0000(0)	0.26282(5)	0.51239(13)	0.1625(3)	0.3597(2)	0.0949(2)
z	0.0000(0)	0.11466(17)	0.2500(0)	0.2500(0)	0.5454(7)	0.6457(5)
Uiso	0.00625(19)	0.0062(4)	0.0086(2)	0.0127(9)	0.0097(7)	0.0104(6)
			6.36(5) GPa			
x	0.0000(0)	0.0000(0)	0.0000(0)	0.0000(0)	0.0000(0)	0.0000(0)
y	0.0000(0)	0.26311(7)	0.51202(17)	0.1637(4)	0.3596(3)	0.0934(3)
z	0.0000(0)	0.1147(2)	0.2500(0)	0.2500(0)	0.5458(8)	0.6463(6)
Uiso	0.0045(2)	0.0047(3)	0.0068(6)	0.0090(11)	0.0079(9)	0.0069(7)
			7.27(9) GPa			

x	0.0000(0)	0.0000(0)	0.0000(0)	0.0000(0)	0.0000(0)	0.0000(0)
y	0.0000(0)	0.26322(8)	0.51246(19)	0.16323(48)	0.35978(32)	0.09462(32)
z	0.0000(0)	0.11484(24)	0.2500(0)	0.2500(0)	0.54612(93)	0.64607(74)
Uiso	0.00614(38)	0.00632(30)	0.00785(47)	0.01116(113)	0.00955(81)	0.01034(90)

8.48(5) GPa

x	0.0000(0)	0.0000(0)	0.0000(0)	0.0000(0)	0.0000(0)	0.0000(0)
y	0.0000(0)	0.26344(7)	0.51226(16)	0.16275(40)	0.36024(27)	0.09409(28)
z	0.0000(0)	0.11456(22)	0.2500(0)	0.2500(0)	0.54675(82)	0.64590(64)
Uiso	0.00475(34)	0.00553(27)	0.00693(43)	0.00975(102)	0.00773(68)	0.00856(74)

9.97(19) GPa

x	0.0000(0)	0.0000(0)	0.0000(0)	0.0000(0)	0.0000(0)	0.0000(0)
y	0.0000(0)	0.26346(7)	0.51243(16)	0.16336(42)	0.35995(26)	0.09387(28)
z	0.0000(0)	0.11538(21)	0.2500(0)	0.2500(0)	0.54638(81)	0.64658(60)
Uiso	0.00515(33)	0.00547(25)	0.00625(40)	0.01095(97)	0.00861(69)	0.00848(74)

11.63(7) GPa

x	0.0000(0)	0.0000(0)	0.0000(0)	0.0000(0)	0.0000(0)	0.0000(0)
y	0.0000(0)	0.26374(8)	0.51234(18)	0.1638(5)	0.3599(3)	0.0933(3)
z	0.0000(0)	0.1146(2)	0.2500(0)	0.2500(0)	0.5456(9)	0.6471(7)
Uiso	0.0055(2)	0.0060(3)	0.0069(6)	0.0093(12)	0.0090(10)	0.0090(8)

12.62(5) GPa

x	0.0000(0)	0.0000(0)	0.0000(0)	0.0000(0)	0.0000(0)	0.0000(0)
y	0.0000(0)	0.26391(8)	0.51263(18)	0.16288(45)	0.36036(30)	0.09342(31)
z	0.0000(0)	0.11506(25)	0.2500(0)	0.2500(0)	0.54616(97)	0.64622(73)
Uiso	0.00585(36)	0.00595(27)	0.00747(46)	0.00985(111)	0.00822(74)	0.00961(85)

13.98(10) GPa

x	0.0000(0)	0.0000(0)	0.0000(0)	0.0000(0)	0.0000(0)	0.0000(0)
y	0.0000(0)	0.26393(8)	0.51264(18)	0.1634(5)	0.3601(3)	0.0924(3)
z	0.0000(0)	0.1148(2)	0.2500(0)	0.2500(0)	0.5456(9)	0.6471(7)
Uiso	0.0054(2)	0.0059(3)	0.0067(7)	0.0104(13)	0.0069(11)	0.0080(9)

16.09(7) GPa

x	0.0000(0)	0.0000(0)	0.0000(0)	0.0000(0)	0.0000(0)	0.0000(0)
y	0.0000(0)	0.26426(8)	0.51287(18)	0.1638(5)	0.3604(3)	0.0927(3)
z	0.0000(0)	0.1149(2)	0.2500(0)	0.2500(0)	0.5461(10)	0.6475(7)
Uiso	0.0055(3)	0.0061(3)	0.0068(7)	0.0112(12)	0.0079(11)	0.0083(8)
			17.06(5) GPa			
x	0.0000(0)	0.0000(0)	0.0000(0)	0.0000(0)	0.0000(0)	0.0000(0)
y	0.0000(0)	0.26429(8)	0.51283(19)	0.16343(49)	0.36063(29)	0.095239(33)
z	0.0000(0)	0.11474(28)	0.2500(0)	0.2500(0)	0.54637(105)	0.64775(78)
Uiso	0.00600(40)	0.00686(29)	0.00723(50)	0.00986(121)	0.00801(82)	0.01034(95)

[1]Deposit item: CIF

Table 3. EoS parameters resulting from second order Birch-Murnaghan equation of state fits of unit-cell volume and lattice parameters vs pressure for $Mg_2Fe_2O_5$. The data for Fe_4O_5 are taken from Lavina et al. (2011).

	$Mg_2Fe_2O_5$	Fe_4O_5
V_0 (Å^3)	352.4(2)	-
K_0 (GPa)	171(4)	185.7
a_0 (Å)	2.8917(11)	
M_a (GPa)	572(16)	
b_0 (Å)	9.736(3)	
M_b (GPa)	583(15)	
c_0 (Å)	12.520(15)	
M_c (GPa)	404(28)	

Table 4. M-O bond distances (Å), M2-O1-M2 angle (°), polyhedral volumes (Å^3), octahedral angle variance (OAV in °) and quadratic elongation (OQE) of the M1 and M2 octahedra at each pressure point.

pressure (GPa)	0.0001(1)	0.70(7)	2.15(8)	3.82(5)	6.36(5)	7.27(9)	8.48(5)	9.97(19)	11.63(7)	12.62(5)	13.98(10)	16.09(7)	17.06(5)
M1-O3(x2)	2.048(12)	2.045(8)	2.046(8)	2.025(8)	2.022(8)	2.021(9)	2.008(8)	2.012(9)	2.005(9)	1.992(9)	1.999(9)	1.992(9)	1.992(10)
M1-O2(x4)	2.069(4)	2.067(3)	2.064(4)	2.057(3)	2.047(3)	2.047(4)	2.041(3)	2.037(3)	2.031(4)	2.027(4)	2.021(3)	2.017(4)	2.013(4)
<M1-O>	2.062(7)	2.060(2)	2.058(2)	2.046(2)	2.038(2)	2.036(3)	2.030(2)	2.029(2)	2.023(2)	2.015(3)	2.014(2)	2.009(3)	2.006(3)
V_{M1}	11.653(66)	11.616(40)	11.584(45)	11.380(40)	11.275(47)	11.211(47)	11.130(39)	11.103(42)	11.002(47)	10.873(46)	10.863(42)	10.784(46)	10.744(49)
OAV_{M1}	0.00438	0.00470	0.00387	0.00684	0.00546	0.00771	0.00727	0.00534	0.00589	0.00746	0.00476	0.00554	0.00482
OQE M1	1.0019	1.0022	1.0017	1.0024	1.0016	1.0021	1.0016	1.0015	1.0018	1.0017	1.0014	1.0014	1.0012
M2-O1	1.956(5)	1.942(5)	1.939(4)	1.937(5)	1.929(5)	1.919(5)	1.925(5)	1.911(6)	1.909(5)	1.906(5)	1.908(5)	1.895(5)	1.896(5)
M2-O3(x2)	2.032(3)	2.035(3)	2.028(3)	2.028(2)	2.026(3)	2.017(3)	2.014(2)	2.010(3)	2.012(3)	2.002(3)	2.007(3)	2.000(3)	2.000(3)
M2-O2(x2)	2.059(6)	2.061(4)	2.052(5)	2.051(4)	2.040(5)	2.040(5)	2.035(4)	2.034(5)	2.032(5)	2.030(5)	2.027(5)	2.023(5)	2.020(6)
M2-O2	2.228(14)	2.219(10)	2.227(11)	2.192(10)	2.194(11)	2.185(15)	2.190(11)	2.191(11)	2.161(12)	2.169(13)	2.160(11)	2.153(13)	2.153(13)
<M2-O>	2.061(3)	2.059(2)	2.054(2)	2.048(2)	2.043(3)	2.036(3)	2.035(2)	2.032(2)	2.026(3)	2.023(3)	2.023(2)	2.016(3)	2.015(3)
M2-O1-M2	120.72(27)	120.29(25)	120.25(24)	119.80(24)	120.5(26)	119.75(28)	119.69(24)	119.76(27)	119.87(27)	119.17(27)	119.74(28)	119.41(27)	119.33(28)
V_{M2}	11.491(66)	11.435(42)	11.372(46)	11.257(42)	11.172(48)	11.074(54)	11.064(41)	10.995(47)	10.919(46)	10.862(49)	10.853(46)	10.754(49)	10.742(52)
OAV_{M2}	0.02703	0.02662	0.02799	0.02462	0.02476	0.02553	0.02528	0.02704	0.02403	0.02627	0.02412	0.02516	0.02457
OQE M2	1.0122	1.0132	1.0127	1.0129	1.0126	1.0126	1.0122	1.0129	1.0118	1.0127	1.0120	1.0117	1.0114

M3-O1(x2)	2.059(4)	2.057(3)	2.051(3)	2.045(3)	2.043(3)	2.039(4)	2.031(3)	2.028(3)	2.030(3)	2.017(3)	2.015(4)	2.013(3)	2.008(4)
M3-O3(x4)	2.221(7)	2.209(5)	2.201(5)	2.194(5)	2.172(5)	2.177(6)	2.171(5)	2.162(5)	2.149(6)	2.152(6)	2.139(6)	2.131(6)	2.125(6)
<M3-O>	2.167(3)	2.159(2)	2.151(2)	2.144(2)	2.129(2)	2.131(2)	2.124(2)	2.117(2)	2.109(2)	2.107(2)	2.098(2)	2.092(2)	2.086(2)
V_{M3}	9.57(99)	9.44(93)	9.34(90)	9.25(93)	9.08(91)	9.07(91)	9.00(91)	8.90(85)	8.78(89)	8.77(88)	8.65(88)	8.55(86)	8.47(83)

329 **Table 5.** Resulting elastic parameters from the linearized BM2 EoS fits of the individual M-O
330 bond distances.

	M1-O2	M1-O3	M2-O1	M2-O2	M2-O2b	M2-O3	M3-O1	M3-O3
$d_{0,measured}$ (Å)	2.069(4)	2.048(12)	1.956(5)	2.059(6)	2.228(14)	2.032(3)	2.059(4)	2.221(7)
$d_{0,EoSfit}$ (Å)	2.071(2)	2.049(5)	1.950(3)	2.060(2)	2.230(7)	2.036(2)	2.060(2)	2.217(3)
M_0 (GPa)	517(33)	447(63)	484(43)	753(77)	363(58)	782(60)	587(39)	323(22)

331 **Figure 1**

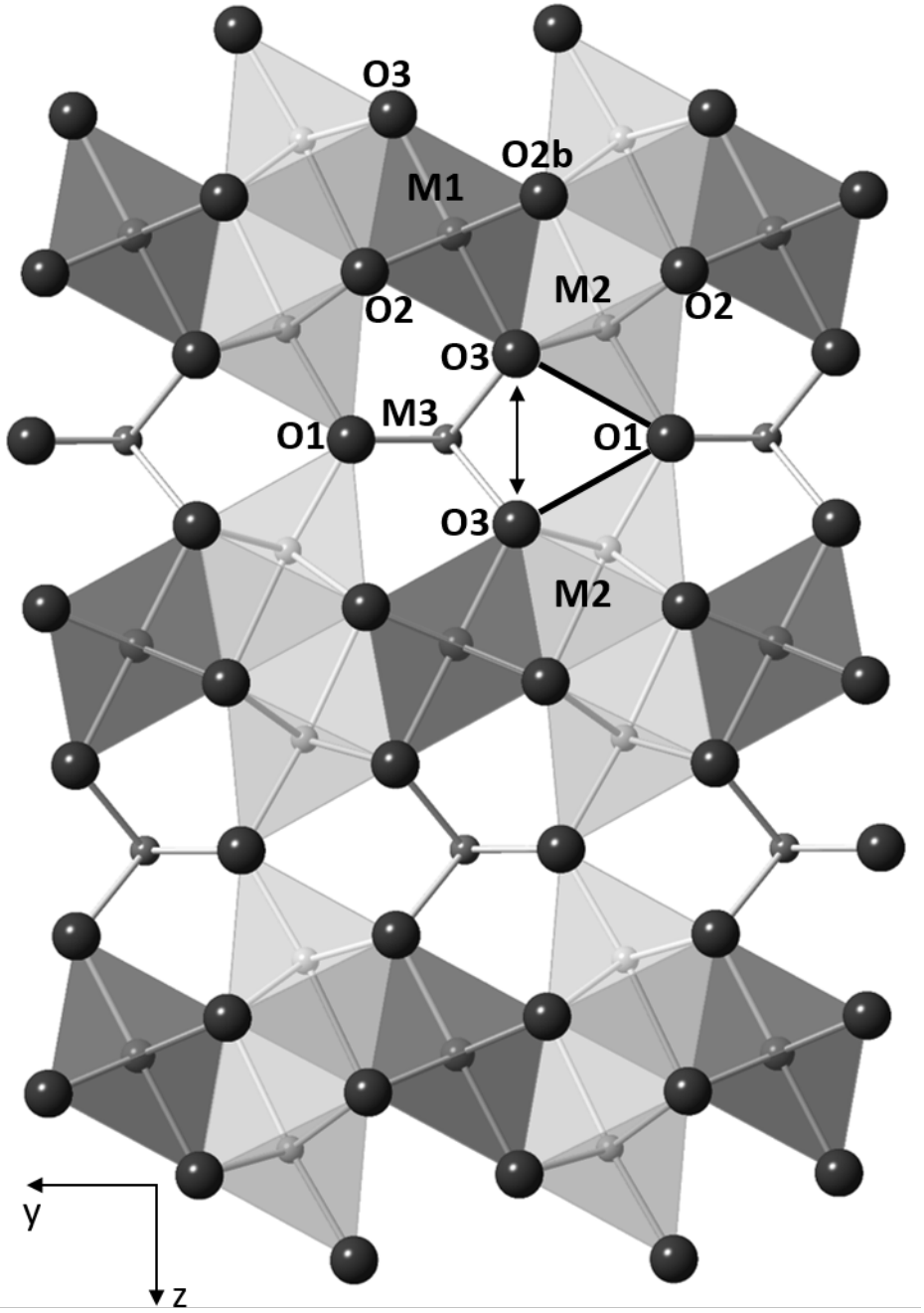

Figure 1

332

333

This is a preprint, the final version is subject to change, of the American Mineralogist (MSA)
Cite as Authors (Year) Title. American Mineralogist, in press.
(DOI will not work until issue is live.) DOI: http://dx.doi.org/10.2138/am-2017-5837

334 **Figure 2a**

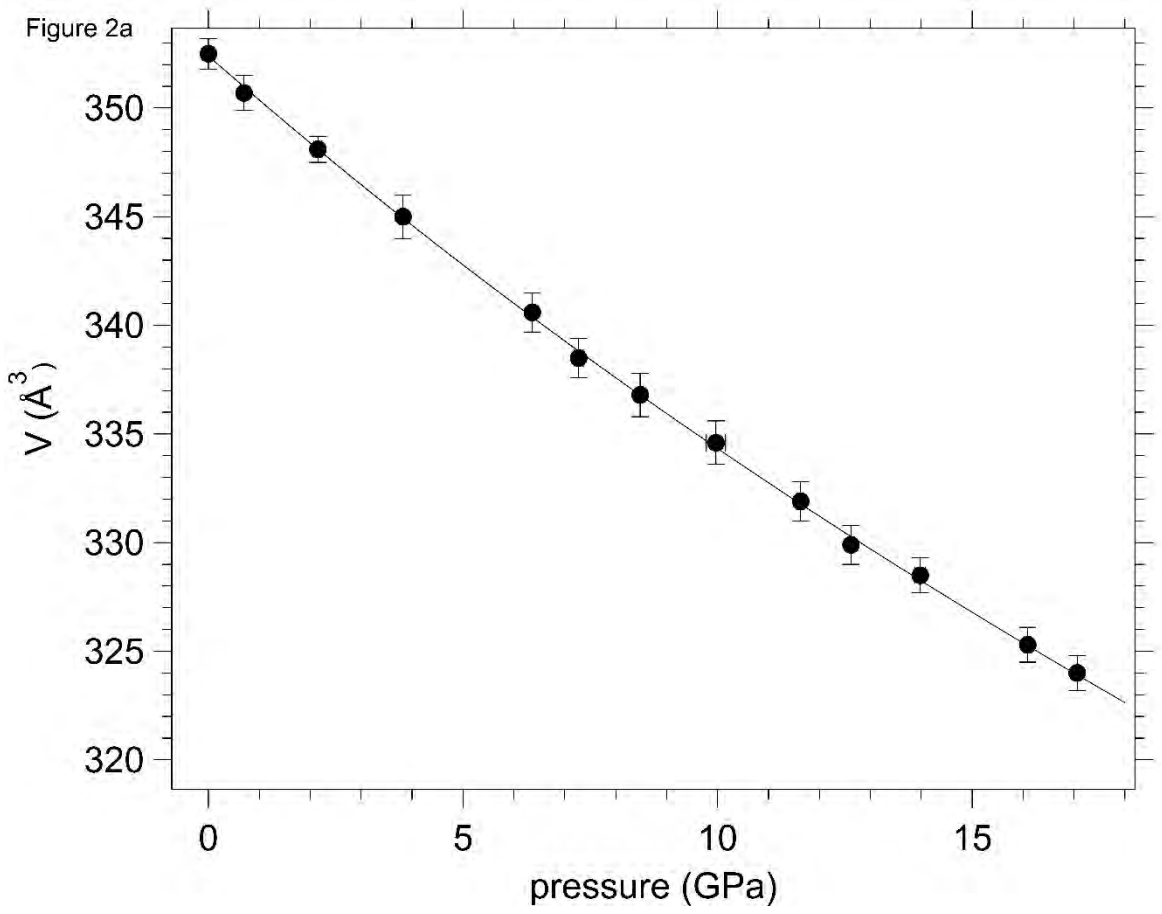

335

336

337 **Figure 2b**

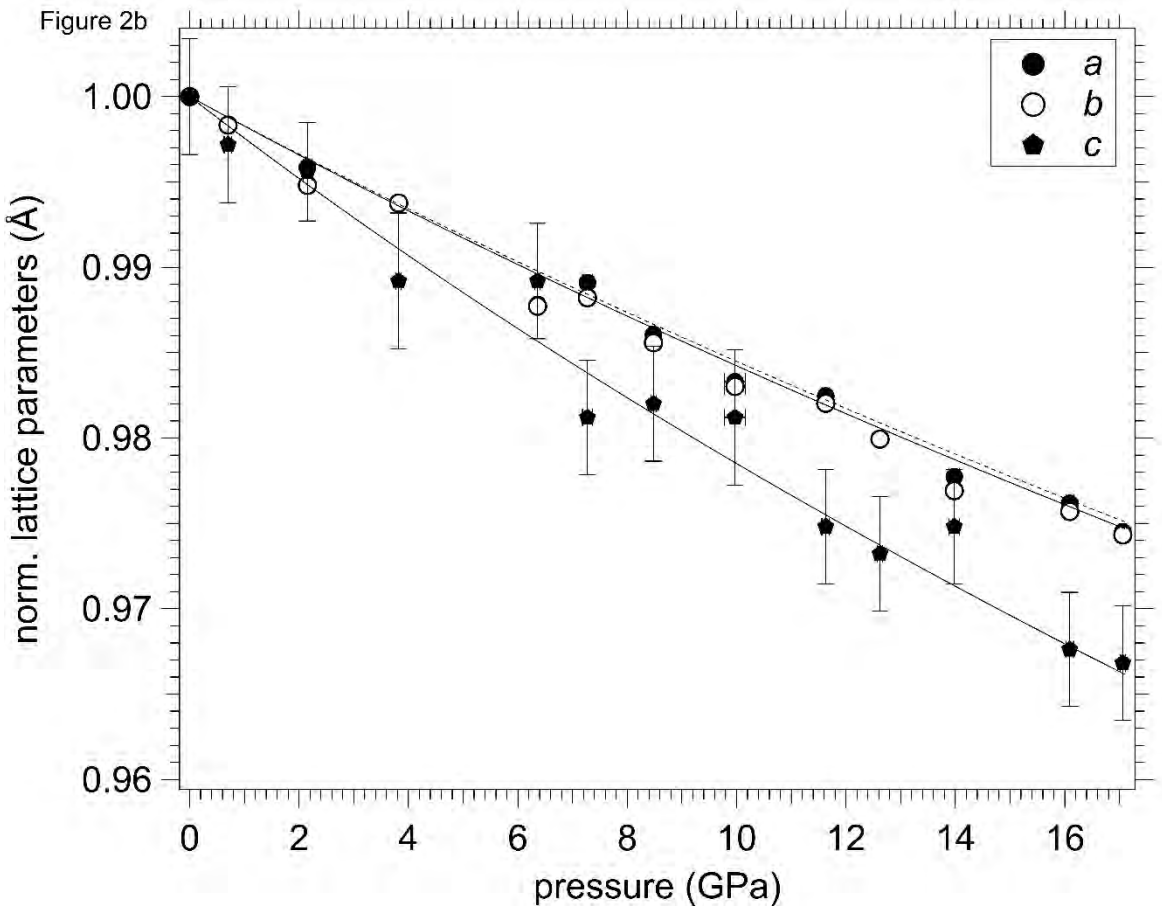

338

339

340 **Figure 3**

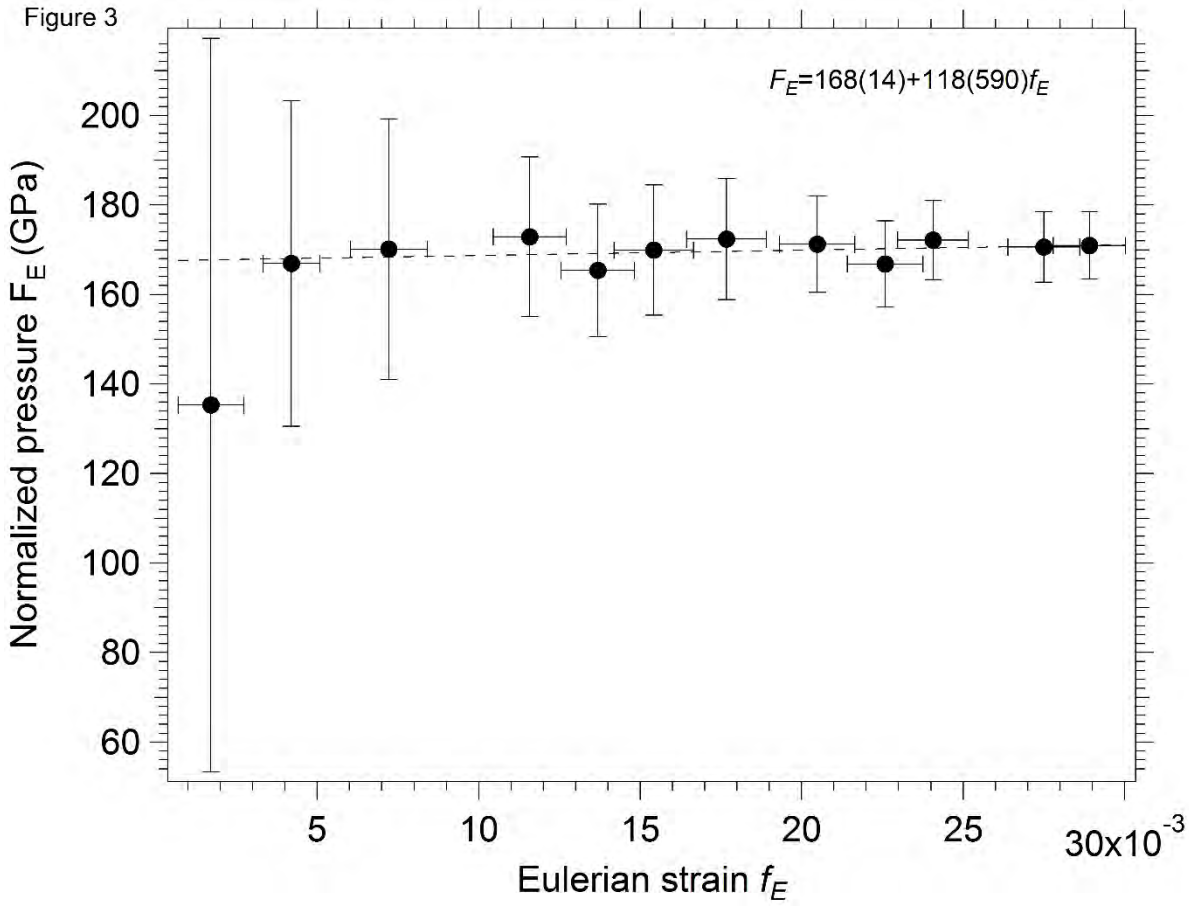

341

342

343 **Figure 4a**

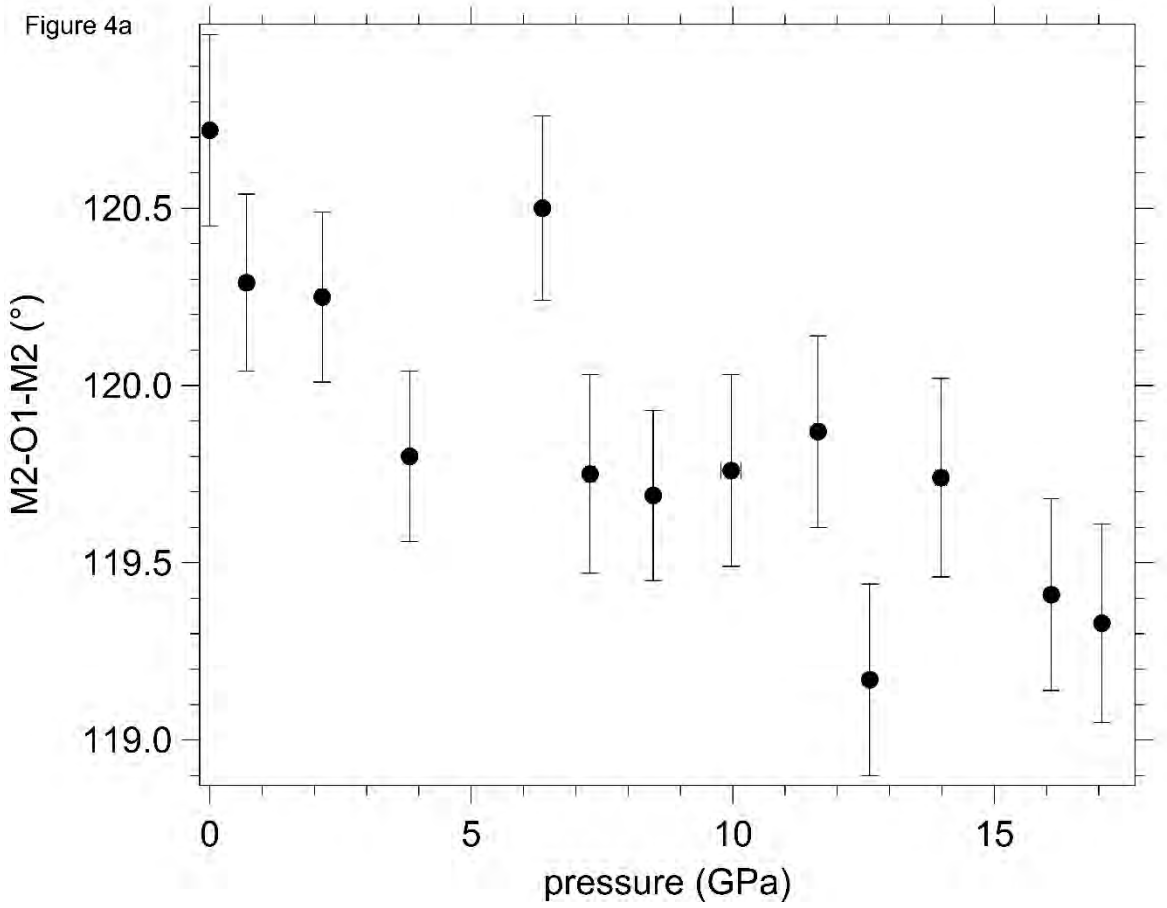

344

345

346 **Figure 4b**

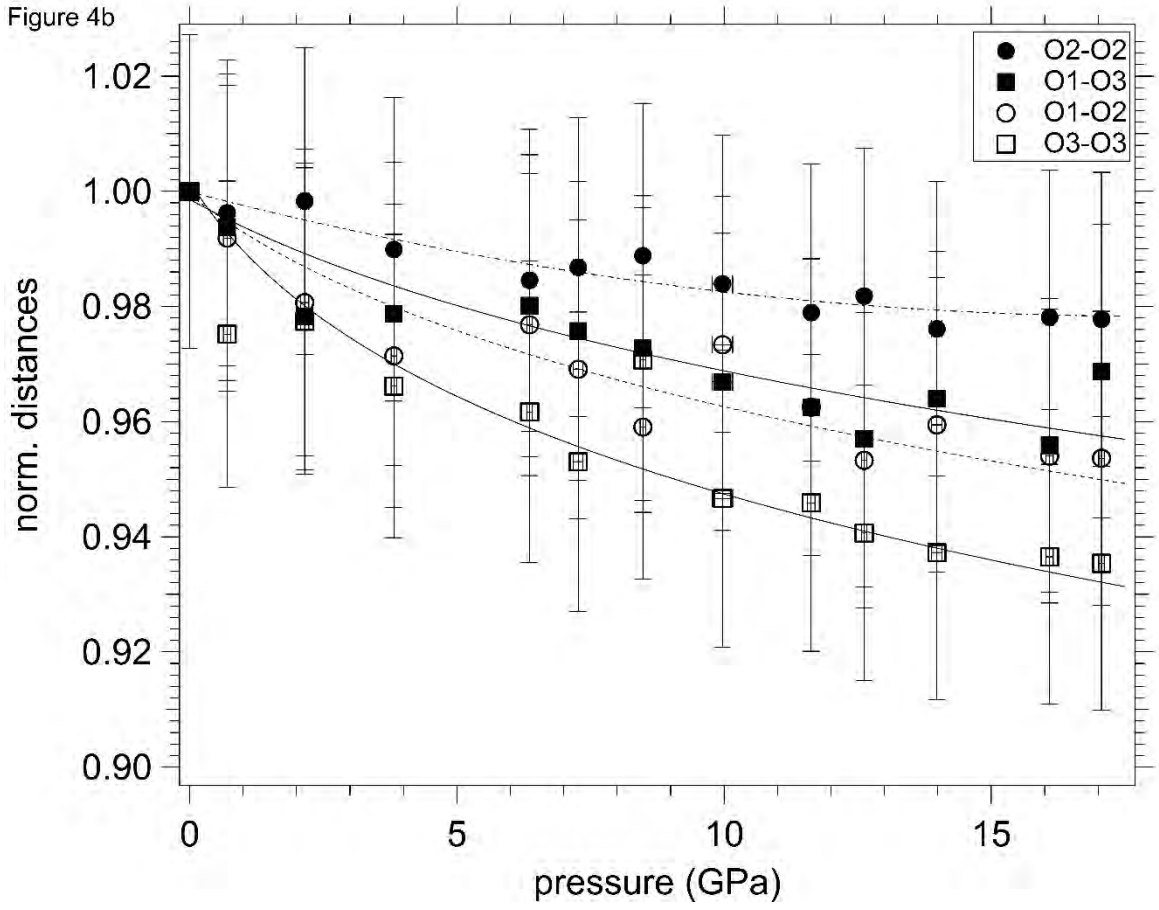

347

348

Figure 5a

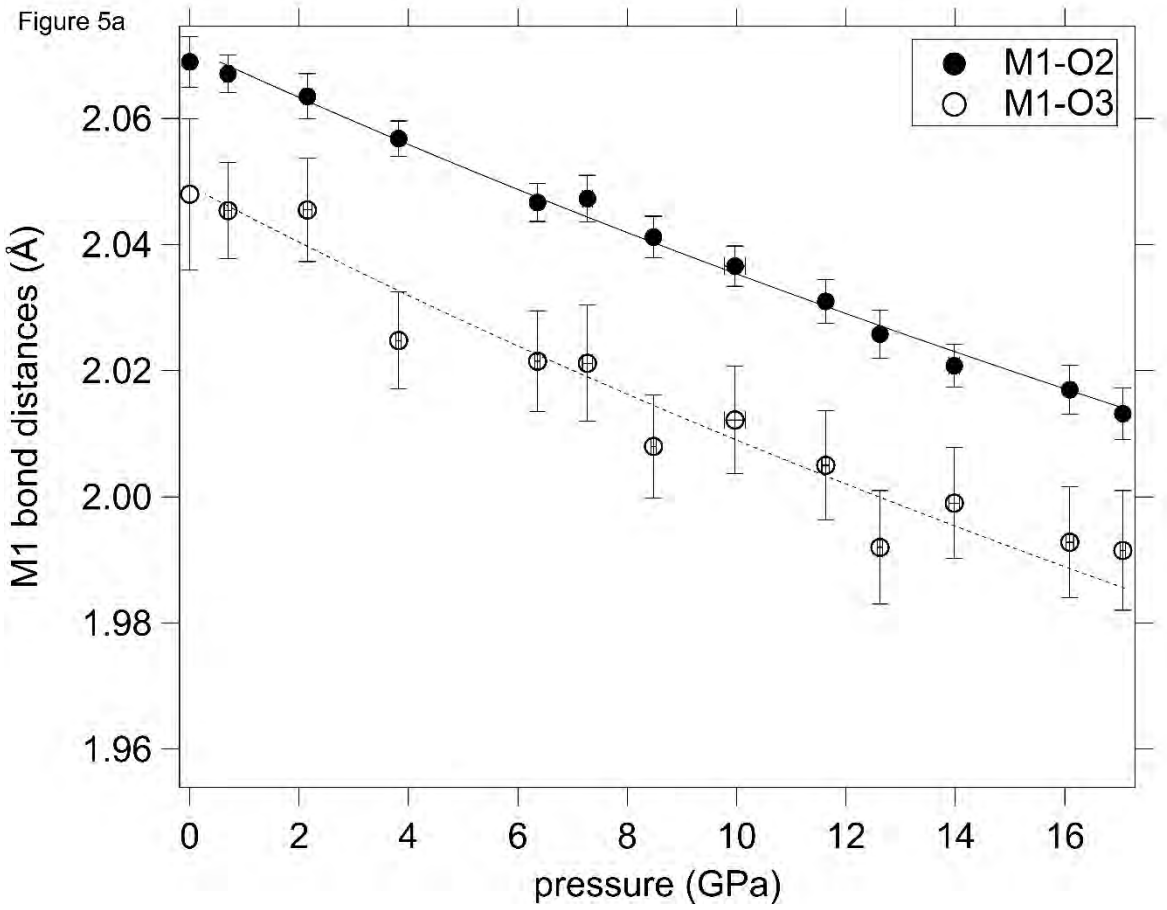

352 **Figure 5b**

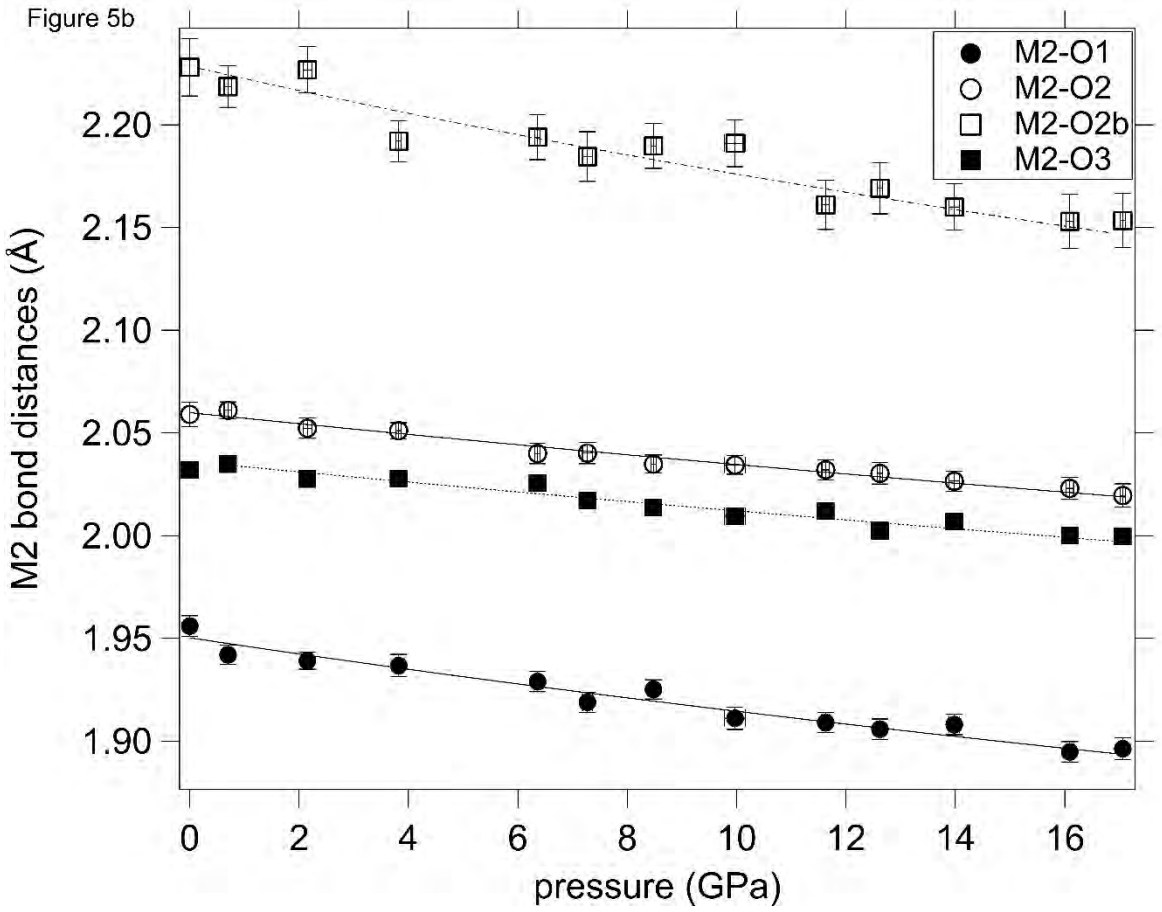

353

354

355 **Figure 5c**

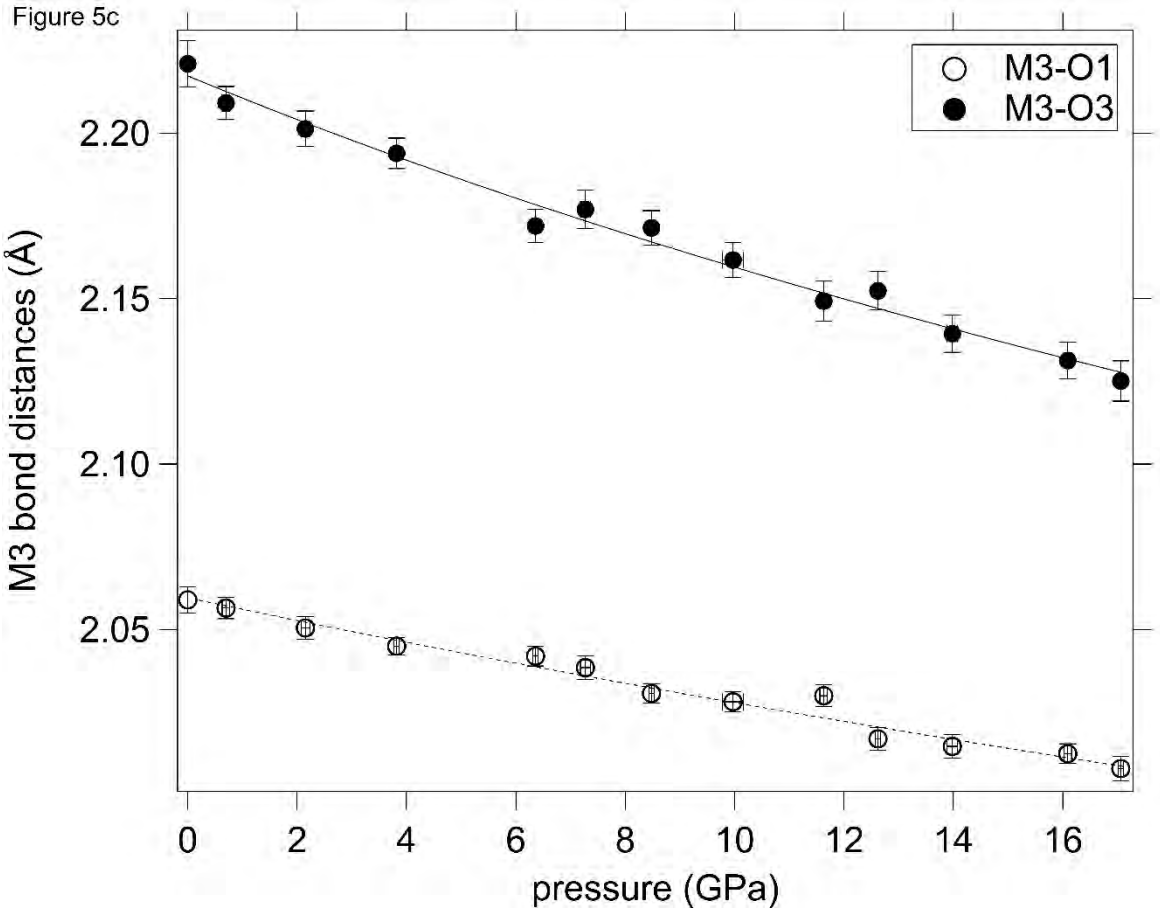

356

This is a preprint, the final version is subject to change, of the American Mineralogist (MSA)
Cite as Authors (Year) Title. American Mineralogist, in press.
(DOI will not work until issue is live.) DOI: http://dx.doi.org/10.2138/am-2017-5837

357 **Figure 6**

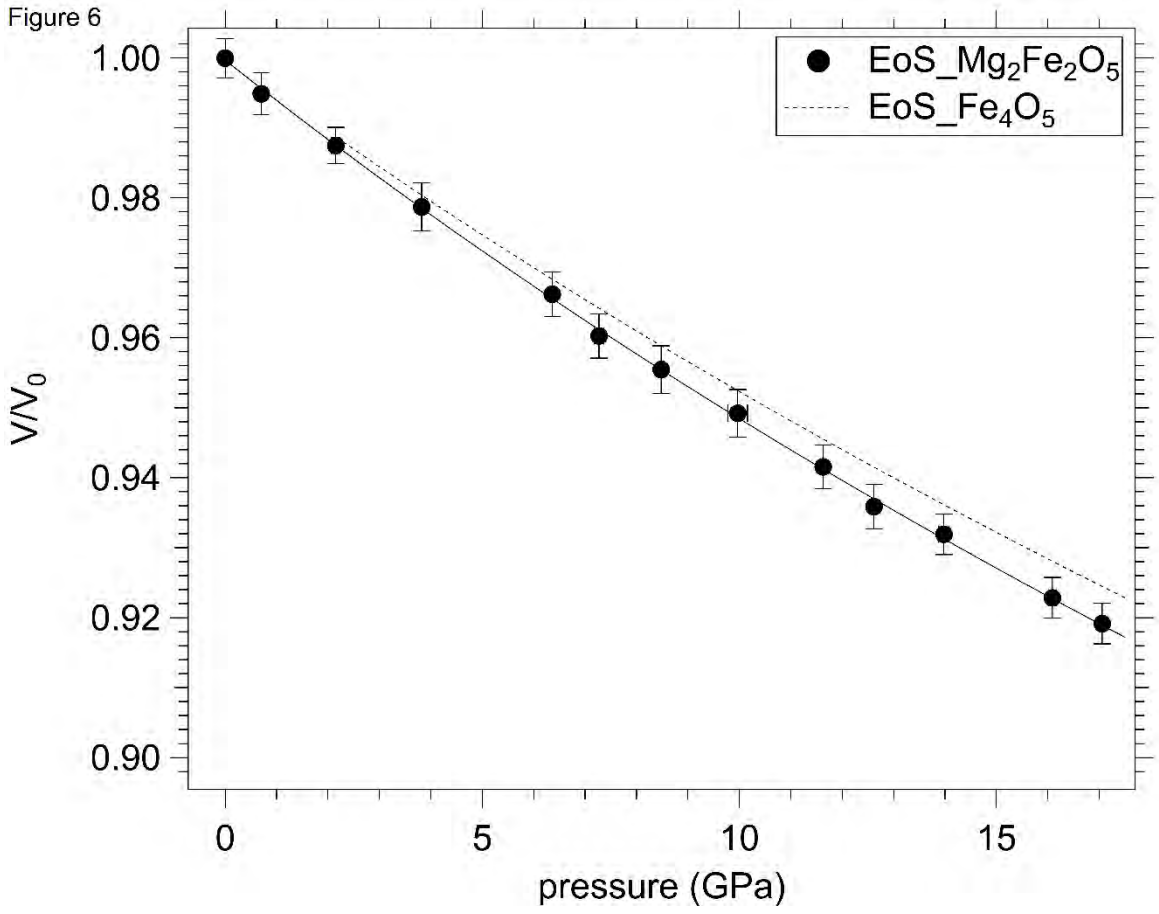

358